






Research Article

Reduction of bias for sparsity promoting regularization in MPI

Lina Nawwas ^{a,b,*}, Christina Brandt ^c, Patryk Szwargulski ^{a,b}, Tobias Knopp ^{a,b},
Martin Möddel ^{a,b}

^aSection for Biomedical Imaging, University Medical Center Hamburg-Eppendorf, Hamburg, Germany

^bInstitute for Biomedical Imaging, Technical University Hamburg, Hamburg, Germany

^cDepartment of Mathematics, University of Hamburg, Hamburg, Germany

*Corresponding author, email: l.nawwas@uke.de

Received 16 October 2020; Accepted 09 November 2021; Published online 17 December 2021

© 2021 Nawwas *et al.*; licensee Infinite Science Publishing GmbH

This is an Open Access article distributed under the terms of the Creative Commons Attribution License (<http://creativecommons.org/licenses/by/4.0>), which permits unrestricted use, distribution, and reproduction in any medium, provided the original work is properly cited.

Abstract

Magnetic Particle Imaging (MPI) is a tracer based medical imaging modality with great potential due to its high sensitivity, high spatial and temporal resolution, and its ability to quantify the tracer concentration. Image reconstruction in MPI is an ill-posed problem, which can be addressed by regularization methods that lead to a reconstruction bias, which is apparent in a systematic mismatch between true and reconstructed tracer distribution. This is expressed in a background signal, a mismatch of the spatial support of the tracer distribution and a mismatch of its values. In this work, MPI reconstruction bias and its impact are investigated and a recently proposed debiasing method with significant bias reduction capabilities is adopted.

1. Introduction

Magnetic Particle Imaging (MPI) is a tracer-based tomographic imaging technique able to recover the spatial distribution of the tracer [1]. It has been shown to achieve good spatial (< 1 mm) [2] and excellent temporal resolution (e.g., as much as 4 mL could be imaged at a rate of 46 volumes per second) [3] and like MRI, does not involve any ionizing radiation, but instead uses magnetic fields to perform its measurement. In the setups MPI is currently used, the relation between tracer concentration and MPI signal intensity is linear and image reconstruction is an ill-posed inverse problem [4–6]. In practice, this can lead to large variances in the reconstructed images stemming from measurement noise. A well established method to reduce the impact of noise is regularization [7, 8], which improves the robustness of the reconstruction algorithm by trading off variance

and bias in such a way that the biased regularized reconstruction outperforms the unbiased one. Bias here refers to a systematic deviation of the reconstruction result compared to the true data. This can for instance be an over- or under-estimation of the tracer concentration or certain artifact pattern in the reconstructed image. In MPI, Tikhonov regularization was the first type of regularization to successfully improve imaging quality [4] and it is still commonly in use. More recent additions were total variation (TV), ℓ^1 regularization [9] and structural a priori information based regularization [10].

One of the most interesting properties of MPI is that it provides quantitative information about the tracer distribution. This leads to a wide range of potential medical applications, such as the quantification of vascular stenosis [11, 12], perfusion imaging [13–15], assessment of aneurysm hemodynamics [16], blood flow measurements [17], quantification of stem cells [18], and cerebral

blood volume measurements [19]. It is also essential for multi-contrast MPI applications [20], such as temperature mapping [21], viscosity quantification [22] and nanoparticle core size discrimination [23]. Reconstruction bias can potentially lead to a systematic error in such applications, as e.g. recognized by Vallma et al. [12] for the quantification of vascular stenosis. Thus, bias in general can be problematic for applications requiring an accurate quantification of the particle concentration. In other imaging modalities such as PET/CT this issue has already been addressed [24]. MPI reconstruction artifacts were first investigated in [25]. However, there has not yet been a systematic investigation of bias in MPI.

A first aim of this work is to investigate the image reconstruction bias for MPI and the potential impact on its quantifiability for TV and ℓ^1 regularization. There are two straight forward approaches to reduce the impact of bias. One can use a calibration based approach for quantification, where the bias is taken into account by using reference measurements - An approach used, for instance, for viscosity quantification [22]. A more generic approach can be the use of regularization methods, which introduce less bias to begin with. In this work, we take the latter and adopt a recently introduced two-step debiasing method [26] because it is more general and potentially able to reduce bias for a wide variety of applications. We compare regular TV and ℓ^1 regularization with their debiased counterparts using simulated data and assess the potential impact on quantitative applications using an exemplary experimental application.

II. Problem statement

The basic principle of MPI is based on the nonlinear magnetization response of magnetic nanoparticles [1, 2, 27]. A static selection field saturates all particles except for those in the vicinity of the field-free region. A dynamic drive field is applied to rapidly move this region within the field of view of the MPI scanner. Inductive receive coils pick up changes of the nanoparticle magnetization. The relation between the particle distribution and the measured signal can be described by a linear system of equations

$$Sc = u, \quad (1)$$

where $u \in \mathbb{C}^M$ are the Fourier coefficients of the induced signal, $S \in \mathbb{C}^{M \times N}$ is the system matrix, and $c \in \mathbb{R}_+^N$ is the concentration vector. The latter holds N concentration values describing the spatial distribution of the magnetic nanoparticles. More details on the formulation of the MPI image reconstruction problem can be found in [28].

MPI aims to obtain the unknown concentration vector c , given a measured signal u , which is typically obtained by minimizing the Tikhonov functional

$$c_\alpha \in \arg \min_c \frac{1}{2} \|Sc - u\|_2^2 + \alpha J(c), \quad (2)$$

with regularization functional J and regularization parameter α , which controls the effect of the regularization functional.

Regularization methods in general suffer from bias, which can be divided into two parts, model bias and method bias [26]. The former is due to the choice of the regularization method and is unavoidable. The latter is a systematic error due to the weight on the regularization and can be corrected. The most commonly used regularization functional in MPI is the classical Tikhonov regularization, i.e., the ℓ^2 norm. The first row of Figure 1 shows the reconstruction of two different one-dimensional tracer distributions with a Tikhonov regularization functional as well as the original tracer distributions which are generated by an MPI system matrix based forward simulation. Signals in the first row are reconstructed using Kaczmarz algorithm. Both signals are over-smoothed, blurred and the first one suffers from overshooting on the edges. Those structural artifacts are considered to be the model bias of Tikhonov regularization. Since this part of bias cannot be avoided, other regularization functionals were considered, such as, TV and ℓ^1 [9]. The former is chosen for the steps signal as it preserves the edges [29], while the latter has the advantage of enforcing sparsity [30], which makes it a suitable choice for the sparse signal. The second row of Figure 1 displays the MPI simulated one-dimensional signals reconstructed with the first order primal dual algorithm using TV and ℓ^1 regularization functionals, respectively. It is clear that the structure of the signals is recovered better but they suffer from under-estimation, which can be seen as a drop in height of the steps in the first signal and as a shrinkage of the peak values in the second one. This under-estimation is related to the method bias, which we aim to correct using the two-step debiasing method.

III. Theory

III.1. The two-step debiasing method

The main idea of the two-step debiasing method [26] for variational regularization is based on determining the support of the true solution by solving the standard variational problem in a first step. Then, the second debiasing step minimizes the data fidelity term on the same support with a zero Bregman distance [31] constraint. The definition of the Bregman distance depends on the subgradient obtained from the optimality condition of the variational problem. It is shown in [26] that the two-step debiasing method is well-defined, applicable for a wide range of regularization functionals and optimally reduces the bias.

The first step of the two-step debiasing method is to consider the solution of the variational problem (2) and

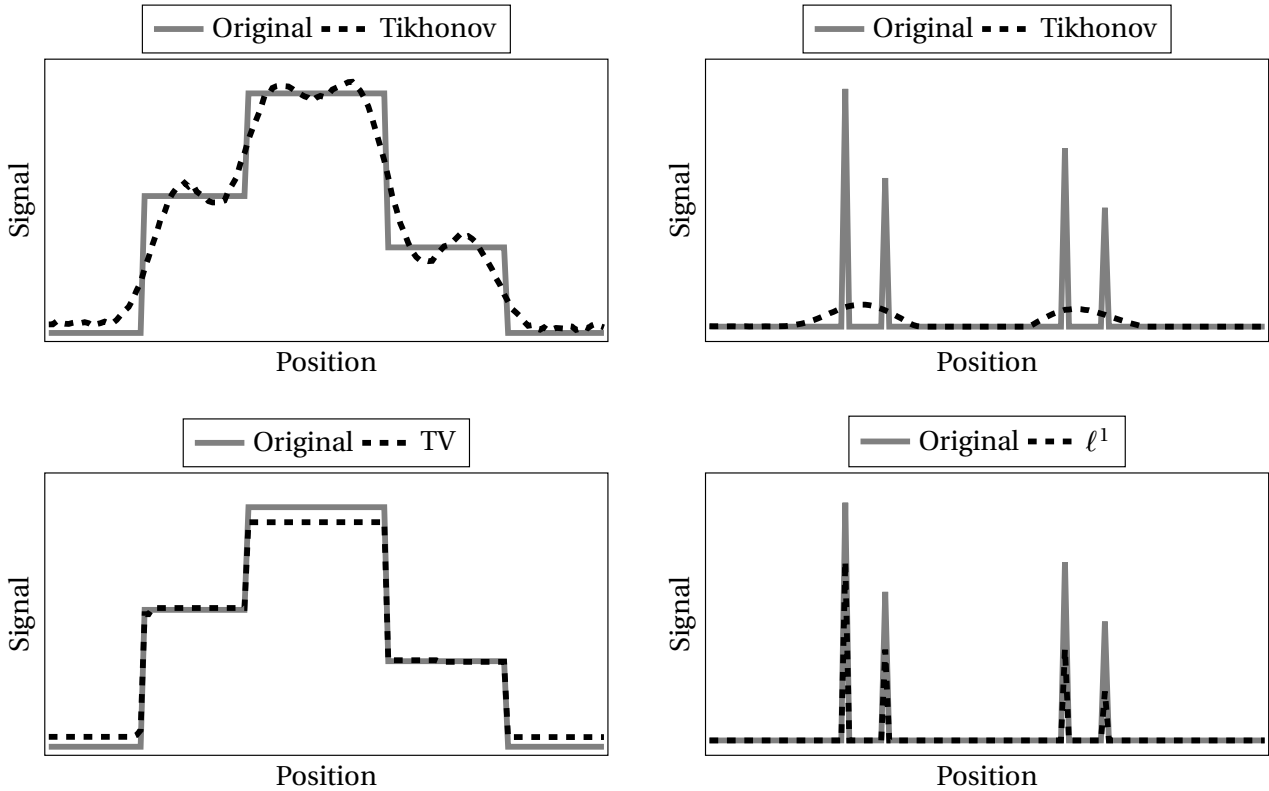


Figure 1: Tikhonov (left and right top), TV (left bottom) and ℓ^1 (right bottom) reconstructions (black, dashed) of one-dimensional signals (dark gray, solid) show model bias as over smoothing (Tikhonov) and method bias as signal reduction (TV and ℓ^1).

compute its first-order optimality condition

$$S^*(Sc_\alpha - u) + \alpha p_\alpha = 0, \quad p_\alpha \in \partial J(c_\alpha), \quad (3)$$

where S^* is the adjoint of the operator S , and p_α is the subgradient, which carries over information about c_α to the second step. Proceeding to the second debiasing step, it minimizes the data fidelity term over the set of all c sharing the support of c_α . This sharing support condition can be reformulated as a vanishing Bregman distance between c and c_α

$$\hat{c}_\alpha \in \arg \min_c \frac{1}{2} \|Sc - u\|_2^2 \text{ s.t. } D_f^{p_\alpha}(c, c_\alpha) = 0, \quad (4)$$

with the Bregman distance [8] defined as

$$D_f^p(u, v) = J(u) - J(v) - \langle p, u - v \rangle, \quad p \in \partial J(v).$$

We assume J to be absolutely one-homogeneous, i.e., $J(\lambda c) = |\lambda|J(c)$ for all $\lambda \in \mathbb{R}$. Then, the Bregman distance reduces to

$$D_f^p(u, v) = J(u) - \langle p, u \rangle, \quad p \in \partial J(v).$$

In summary, the steps of the two-step debiasing method are given by:

1. Compute the (biased) solution c_α of (2) with optimality condition (3).
2. Compute the (debiased) solution \hat{c}_α as the minimizer of (4).

III.II. Numerical implementation using the first-order primal dual algorithm

In the previous section, we discussed the two-step debiasing method to find a variationally regularized reconstruction of the true signal with reduced method bias. The method requires solving the two minimization problems (2) and (4), which can be reformulated as

$$\min_c \frac{1}{2} \|Sc - u\|_2^2 + \alpha J(c), \quad (5)$$

$$\min_c \frac{1}{2} \|Sc - u\|_2^2 + \gamma D_f^{p_\alpha}(c, c_\alpha). \quad (6)$$

For solving those minimization problems, we use the first-order primal dual algorithm [32, 33] due to its simplicity and ability to update both the primal and dual variables in each iteration. In the following, we derive the algorithm for a more general setting and later map it to the specific optimization function in section III.III. Starting point is the general form of the minimization problems considered in this work, i.e., primal problems of the form

$$\min_{c \in X} \{F(Ac) + H(c)\}, \quad (7)$$

where $A: X \rightarrow Y$ is a continuous linear operator between Hilbert spaces and $F: Y \rightarrow \mathbb{R}_\infty := \mathbb{R} \cup \{+\infty\}$ as well as

$H : Y \rightarrow \mathbb{R}_\infty$ are convex, proper, lower semicontinuous (l.s.c) functions. In our setting, Y is a product space of Hilbert spaces, i.e., $Y = Y_1 \times Y_2$, and we write $y = (y_1, y_2)$ with $y_i \in Y_i$ for $i = 1, 2$. Consequently, we have $(Ac)_i = A_i c$ with $A_i : X \rightarrow Y_i$ for $i = 1, 2$. Moreover, we assume that F is separable, i.e., $F(y) = F_1(y_1) + F_2(y_2)$.

Instead of solving the primal problem (7), one uses the duality principle to derive the dual or the saddle point problem with help of the Fenchel conjugate [34]. The Fenchel conjugate of a function $G : Y \rightarrow \mathbb{R}_\infty$ is given by $G^* : Y \rightarrow \mathbb{R} \cup \{-\infty, \infty\}$,

$$G^*(y) := \max_{z \in Y} \{ \langle z, y \rangle - G(z) \}. \quad (8)$$

The dual and the primal-dual formulations of (7) are thus given by

$$\begin{aligned} & \max_{y \in Y} \{ -(H^*(-A_1^* y_1 - A_2^* y_2) + F_1^*(y_1) + F_2^*(y_2)) \}, \quad (9) \\ & \min_{c \in X} \max_{y \in Y} \{ \langle A_1 c, y_1 \rangle + \langle A_2 c, y_2 \rangle + H(c) \\ & \quad - F_1^*(y_1) - F_2^*(y_2) \}, \quad (10) \end{aligned}$$

where F_1^* , F_2^* , and H^* are the Fenchel conjugates of F_1 , F_2 , and H . Note that we used the separability of F leading to $F^*(y) = F_1^*(y_1) + F_2^*(y_2)$. A saddle point $(\hat{c}, \hat{y}_1, \hat{y}_2)$ of the saddle point problem (10) satisfies the optimality condition

$$\begin{pmatrix} 0 \\ 0 \\ 0 \end{pmatrix} \in \begin{pmatrix} -A_1 \hat{c} + \partial F_1^* \hat{y}_1 \\ -A_2 \hat{c} + \partial F_2^* \hat{y}_2 \\ A_1^* \hat{y}_1 + A_2^* \hat{y}_2 + \partial H(\hat{c}) \end{pmatrix},$$

where ∂F_1^* , ∂F_2^* , and ∂H are the subdifferentials of the convex functions F_1^* , F_2^* , and H .

From that we obtain the first order primal dual algorithm iterations with extrapolation in the primal variable summarized in Algorithm 1.

Algorithm 1 First-Order Primal-Dual Algorithm

Input: u, F_1, F_2, H, A_1, A_2 , and $\alpha > 0$
Initialization: $c^0 = \bar{c}^0 = 0, y_1^0 = y_2^0 = 0, \sigma, \tau > 0$, such that $\sigma \tau L^2 < 1$, where $L = \|A_1\|$
while not converged **do**
 $y_1^{n+1} = (I + \sigma \partial F_1^*)^{-1}(y_1^n + \sigma A_1 \bar{c}^n)$
 $y_2^{n+1} = (I + \sigma \partial F_2^*)^{-1}(y_2^n + \sigma A_2 \bar{c}^n)$
 $c^{n+1} = (I + \tau \partial H)^{-1}(c^n - \tau(A_1^* y_1^{n+1} + A_2^* y_2^{n+1}))$
 $\bar{c}^{n+1} = 2c^{n+1} - c^n$
end while
return $c_\alpha = c^{n+1}$

Stopping Criterion

Concerning the choice of the stopping criterion, we consider the primal-dual gap of the saddle point problem.

The primal-dual gap is simply defined as the difference between the primal and the dual problems for the current values of variables [33]. The iterations of the primal-dual algorithm converge to the saddle point as the primal-dual gap approaches zero. Thus, the algorithm converges if the primal-dual gap is less than a chosen value $\epsilon > 0$.

III.III. TV and ℓ^1 Regularization

For the TV-type regularization we set the regularization functional to $J(c) = \|\Gamma c\|_1$, where Γ is the gradient operator implementing the finite differences. The numerical implementation of the minimization problems requires the system matrix S and the measurement vector u to be real. Given that $c \in \mathbb{R}^N$ is real, we can reformulate the complex system $S c = u$ into a real system $\tilde{S} c = \tilde{u}$ by simple stacking of the real and imaginary parts of S and u , respectively. Then, we get a real-valued system matrix $\tilde{S} \in \mathbb{R}^{2M \times N}$, $\tilde{u} \in \mathbb{R}^{2M}$, and $c \in \mathbb{R}^N$. For simplicity, we keep on using the symbols S , u , and c to represent the system matrix, measurement vector, and the concentration vector, respectively, but notice that from here on they will be in the real space. Generally, $\Gamma \in \mathbb{R}^{D \times N}$ represents a discrete linear gradient operator and $S \in \mathbb{R}^{2M \times N}$ denotes a linear forward operator. Thus, we get the following discrete optimization problems to solve:

$$c_\alpha \in \arg \min_c \underbrace{\frac{1}{2} \|S c - u\|_2^2}_{F_1(Sc)} + \underbrace{\alpha \|\Gamma c\|_1}_{\alpha F_2(\Gamma c)} + \underbrace{\mathbf{I}_+(c)}_{H(c)}, \quad (11)$$

$$\hat{c}_\alpha \in \arg \min_c \underbrace{\frac{1}{2} \|S c - u\|_2^2}_{F_1(Sc)} + \underbrace{\gamma \|\Gamma c\|_1}_{\gamma F_2(\Gamma c)} - \underbrace{\gamma \langle p_\alpha, c \rangle}_{H(c)} + \mathbf{I}_+(c), \quad (12)$$

where $\mathbf{I}_+(c)$ is equal to 0 if $c_{ij} \geq 0$ for all i, j , and equal to ∞ otherwise. $\mathbf{I}_+(c)$ is used to incorporate the non-negativity constraint on c .

From the previous section, we noticed that the first order primal-dual algorithm (Algorithm 1) requires calculating the proximal mappings of the convex conjugate of the data fidelity term and the regularization functional. Recall that the proximal mapping [35] for a real-valued convex function f is defined as

$$(I + \lambda \partial f)^{-1}(\xi) := \arg \min_v \left\{ \frac{\|v - \xi\|_2^2}{2\lambda} + f(v) \right\}. \quad (13)$$

Hence, the convex conjugate of F_1 and βF_2 and the proximity operators of F_1^* , $(\beta F_2)^*$, and H are given by

$$\begin{aligned} F_1^*(y_1) &= \frac{1}{2} \|y_1\|_2^2 + \langle y_1, u \rangle, \\ (\beta F_2)^*(y_2) &= \mathbf{I}_{B_\beta^\infty}(y_2), \\ (I + \sigma \partial F_1^*)^{-1}(\xi) &= \frac{\xi - \sigma u}{1 + \sigma}, \\ (I + \sigma \partial (\beta F_2)^*)^{-1}(\xi) &= \left(\frac{\beta \xi_i}{\max(\beta, |\xi_i|)} \right)_{i=1}^N, \\ (I + \tau \partial H)^{-1}(\xi) &= \max(0, \xi + \tau \gamma p_\alpha), \end{aligned}$$

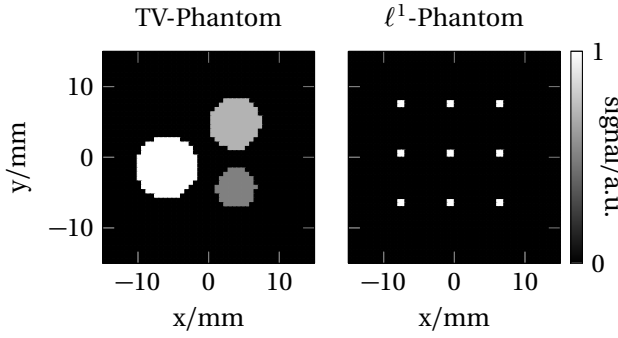


Figure 2: The TV (left) and ℓ^1 (right) simulation phantoms are shown.

where $\mathbf{I}_{B_\beta^\infty}$ is the indicator function on the ball B_β^∞ with β a given scalar and N is the length of the vector ξ . $H(c)$ in the minimization problem (11) has γ equal to 0, which means that the proximity operator for this step would be a positive projection. For detailed information how to compute these convex conjugates and proximity operator, we refer to [36].

Applying the primal dual algorithm (Algorithm 1) to the minimization problems (11) and (12), the iterative algorithm produces a primal-dual sequence c^n that converges to the solution of the standard variational problem c_α (11), which is used in the definition of the unique sub-gradient p_α :

$$p_\alpha = \frac{1}{\alpha} S^*(u - S c_\alpha).$$

Similarly, the second step iterations result in a sequence \hat{c}^n that converges to the debiased solution \hat{c}_α .

Similar to the TV regularization case, we apply the same first-order primal-dual algorithm iterations for the ℓ^1 regularization optimization problem by omitting the gradient operator Γ .

IV. Materials and methods

IV.I. Simulation setup

For numerical analysis of the proposed bias reduction method, first, a 2D simulation study was designed. 2D phantoms were used for analysis of TV and ℓ^1 regularization, respectively as shown in Figure 2. The TV-phantom consists of large, medium and small circles with homogeneous perimag tracer concentrations of $5 \text{ mg}_{\text{Fe}} \text{ mL}^{-1}$, $3.5 \text{ mg}_{\text{Fe}} \text{ mL}^{-1}$ and $2.5 \text{ mg}_{\text{Fe}} \text{ mL}^{-1}$ and radii of 5 mm, 4 mm and 3 mm, respectively. The ℓ^1 -phantom consists of nine equally distanced small dots with a concentration of $5 \text{ mg}_{\text{Fe}} \text{ mL}^{-1}$ and a quadratic base of 2×2 mm each. The values of the concentrations were normalized to 1 through our simulation as we notice in Figure 2.

Our simulations were based on a measured 2D system matrix obtained with a preclinical MPI system (Bruker, Ettlingen, Germany). The drive field amplitudes were $12 \text{ mT } \mu_0^{-1}$ in x - and y -directions and the gradient strength was $G_x = G_y = -1 \text{ T m}^{-1} \mu_0^{-1}$ and $G_z = 2 \text{ T m}^{-1} \mu_0^{-1}$, which results in an effective field of view (FOV) of 24×24 mm. The system matrix was measured on a 30×30 grid on a slightly larger area of 30×30 mm. The delta sample had a size of $1 \times 1 \times 1$ mm and was filled with undiluted perimag (micromod Partikeltechnologie GmbH, Rostock, Germany) with an iron concentration of $5 \text{ mg}_{\text{Fe}} \text{ mL}^{-1}$. In order to reduce background noise in the system matrix, frequency components below 80 kHz were removed [37] yielding a total of 948 frequency components remaining. Forward simulation used the system matrix upsampled using bicubic interpolation by a factor of two in each dimension to avoid committing an inverse crime, whereas reconstructions used the unmodified system matrix. The simulation produces a Fourier domain measurement vector u , which was also filtered by excluding the same frequency components excluded from the system matrix.

The TV-phantom simulation study was run with different noise levels added to the measurement vector u as described in [38] in order to analyze the MPI reconstruction bias effect and its dependence on the noise levels. The noise vector we used is extracted from the system matrix and then upsampled by 5 different values before adding it to the measurement vector.

IV.II. Experimental setup

An additional experimental study was carried out using the preclinical MPI system. The 2D simulation phantoms were used as blueprints to construct 3D measurement phantoms of 4 mm height as shown in Figure 3. All phantoms were filled with perimag using the same iron concentrations as in the simulation study. The 3D MPI measurements were performed using drive fields of $12 \text{ mT } \mu_0^{-1}$ amplitude in all 3 directions and a gradient strength of $G_x = G_y = -1 \text{ mT } \mu_0^{-1}$ and $G_z = 2 \text{ mT } \mu_0^{-1}$ resulting in an effective FOV of $24 \times 24 \times 12$ mm. In total the scanner measured 2000 successive frames that were averaged prior to reconstruction. The corresponding system matrix was taken from the Open MPI Data datasets [39, 40]. It was acquired on a $37 \times 37 \times 37$ grid on a FOV of $37 \times 37 \times 18.5$ mm using a $2 \times 2 \times 1$ mm delta sample filled with undiluted perimag of concentration $5.585 \text{ mg}_{\text{Fe}} \text{ mL}^{-1}$.

IV.III. Image reconstruction

The reconstruction algorithm presented earlier was implemented using the Julia programming language [41]. The algorithm was used to solve the regular reconstruction problem in equation (2) and the corresponding two-

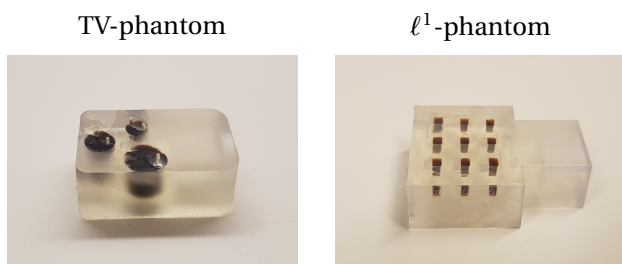


Figure 3: The TV (left) and ℓ^1 (right) measurement phantoms are shown.

step debiasing problem in equation (4) for TV and ℓ^1 regularization functionals. As input parameters, we used step sizes σ and τ equal to 1. Setting σ and τ to 1 was possible due to scaling the system matrix S and measurement vector u with respect to the inverse of the Frobenius norm of the system matrix $\frac{1}{\|S\|_F}$. The stopping criterion parameter ϵ was set to $1 \cdot 10^{-7}$ for the simulated data reconstruction and to $1 \cdot 10^{-10}$ for the experimental data. This choice of ϵ resulted in around 500 primal dual algorithm iterations. For the simulated data, regularization parameters α were chosen to be in the range of $1 \cdot 10^{-4}$ to $1 \cdot 10^0$ for TV, ℓ^1 and the reference Tikhonov (ℓ^2) regularization. For the experimental data, regularization parameters α were chosen to be in the range of $1 \cdot 10^{-6}$ to $1 \cdot 10^{-3}$. The debiasing parameters γ were selected to be in the range of $1 \cdot 10^{-5}$ to $1 \cdot 10^2$ for both the simulated and the experimental data. Lastly, as a reference, the experimental data was reconstructed using standard ℓ^2 Tikhonov regularization, which was handled using the Kaczmarz algorithm implementation from the *MPIReco.jl* package [42] with 10 iterations for the TV-phantom and 100 iterations for the ℓ^1 -phantom.

IV.IV. Bias analysis - simulation setup

Analysis of the bias was done by evaluation of the Normalized root-mean-square deviation (NRMSD) for the simulated data reconstructions, where the phantom is available as ground truth. NRMSD indicates the absolute fit of the reconstructed images to the real phantom. Lower values of NRMSD indicate better fit. For a more fine grained analysis of where bias occurs, we also computed pixel-wise difference maps between reconstructions and the phantom.

Whenever an optimal regularization parameter needed to be chosen in our simulation setup, we automatically tuned the regularization parameters α by minimizing the NRMSD and thus eliminating the need for manual selection at this point. The same was also done for choosing the optimal debiasing parameter γ .

IV.V. Bias analysis - experimental setup

In order to analyze the potential impact of bias onto quantitative MPI applications, we used an exemplary application, where we estimated the iron mass within the central slice (19 of 37) for each substructure of the phantom, so each circle within the TV-phantom and each dot within the ℓ^1 -phantom. This was done by first multiplying each concentration value within slice 19 by the voxel volume of $0.5 \mu\text{L}$ yielding the per voxel iron mass. Iron masses were then obtained by summing up these per voxel iron masses for each substructure. Substructure selection was done by circular masks centered around the phantom center position with radii 5.5 mm, 4.5 mm, 3.5 mm and 2.5 mm for the large circle, medium circle, small circle, and ℓ^1 -dot, respectively. These estimations varied quite significantly depending on the regularization parameter, so we took the middle-sized circle, respectively the central dot as a reference for calibration. Based on this reference, the regularization parameter with the least deviation between true and estimated iron mass was chosen. The reference true iron masses for the small, medium, and large circles of the TV-phantom are $196 \mu\text{g}$, $88 \mu\text{g}$ and $35 \mu\text{g}$ and $10 \mu\text{g}$ for each of the ℓ^1 -phantom dots.

V. Results

V.I. Reconstruction bias in MPI

Regular reconstruction results of the simulation data using the TV regularization with automatically tuned regularization parameters can be seen in the first row of Figure 4 for different noise levels, together with their discrepancy maps in the second row. When the reconstructed images are analyzed, one can see that the general structure of the phantom with its three components is recovered for most noise levels. Some noise artifacts in the corners of the high noise reconstructions are observed. Noise induced degradation of the recovery is most prominent in the phantom's smallest component, which also happens to have the lowest signal strength. Taking the color mapping into account, we see a systematic under-estimation of the signal strength. Closer inspection of the discrepancy maps confirms our earlier observations about the recovery of the general structure of the phantom, as indicated by the high similarity circular regions in the center of the discrepancy maps. However, in addition to the under-estimation of the signal strength in the phantom's area, they also show an over-estimation in most parts of the remaining image, where there should be no signal. This is caused by low level image noise, which is not or only barely visible in the reconstructed images.

Regularization bias in general is a systematic error and its effect is quantified for TV regularization in Fig-

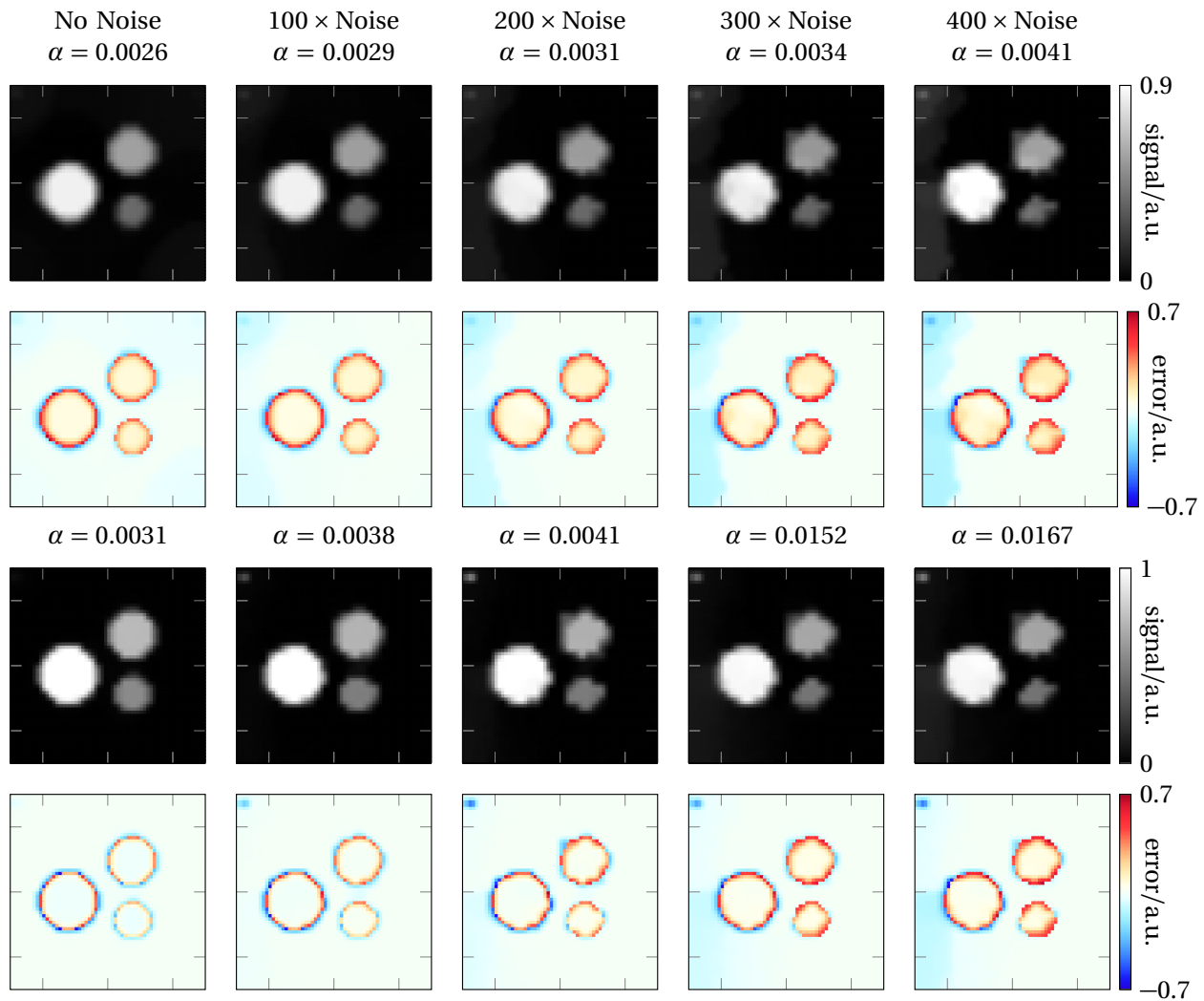


Figure 4: TV regularized reconstruction results of the TV-phantom and the corresponding discrepancy maps for different noise levels using the optimal α value are shown in the two upper rows, respectively. Debiased TV regularized reconstruction results of the TV-phantom and the corresponding discrepancy maps for different noise levels using the optimal α value are shown in the two lower rows, respectively. The blue/red colorbar defines over-estimation in blue and under-estimation in red.

ure 5 (left), where the NRMSD values are plotted as functions of α for each noise level. The minimal NRMSD value increases with increasing the noise, which indicates a bias increase in the reconstructions. Furthermore, we observe a slight shift of the minimum position towards larger α values with increasing noise, which does also occur when choosing the optimal parameter manually based on the visual impression of the images. As far as the visual quality of the reconstructed image is concerned, the regularization parameter minimizing the NRMSD seems to be a good choice for the optimal regularization parameter.

V.II. Bias reduction

Figure 4 shows the debiased reconstruction results of the simulated data and the corresponding discrepancy maps using the automatically tuned α values for each noise level and a fixed γ value of 0.015 in its third and fourth rows, respectively. Visually, the reconstructed images are quite similar to the ones in the first row. In comparison, the signal in the phantom region is more homogeneous for low noise levels and the noise artifacts in some corners are more pronounced for high noise levels. Structure wise, as expected, there are no notable differences. However, we observe that the intensity values are in much better agreement with the phantom. Analyzing the discrepancy maps, we see a large similarity in the image background regions caused by absence of most of

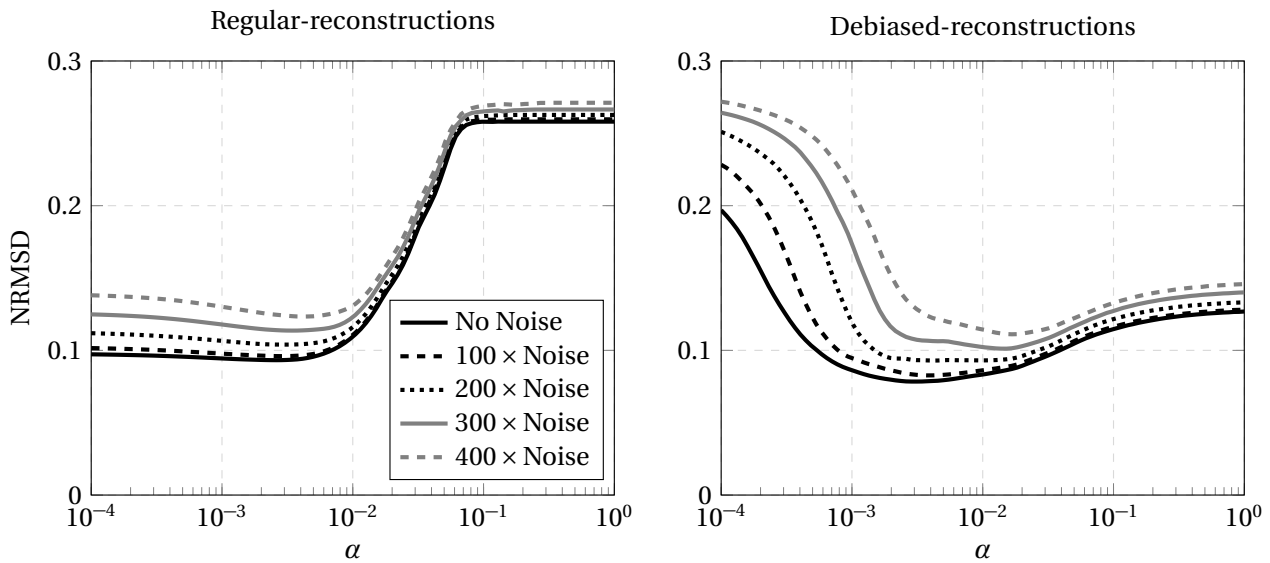


Figure 5: The NRMSD is shown for the regular (left) and the debiased (right) TV reconstructions of the TV-phantom for different noise levels against regularization parameters ranging from $10 \cdot 10^{-4}$ to $1 \cdot 10^0$.

the low strength background noise we observed for the regular reconstruction shown in the first row.

Figure 5 (right) plots the NRMSD values for the debiased reconstruction results for different noise levels and the fixed γ value. In comparison with Figure 5 (left), a decrease in the NRMSD values can be observed. The figure also shows a change in the optimal α values, i.e. the optimal α values for debiasing are different from the ones for the biased case. One can also observe the effect of under- and over-regularization on both regular and debiased reconstructions from Figure 5. Under-regularization affects debiased reconstructions more than regular ones as the debiased reconstructions NRMSD values increase significantly for small α values. Over-regularization has the opposite behaviour, it offers higher NRMSD values for the regular reconstructions than the debiased for large α values.

values smaller than the optimal, the higher the debiasing parameter we use, the worse the reconstructions get. While for α values larger than the optimal, it is better to choose a γ value close to the optimal one or slightly smaller.

V.III. Choice of regularization and debiasing parameter

A detailed analysis on the choice of the regularization parameter α and the debiasing parameter γ is introduced in this section. Figure 6 shows the NRMSD for the debiased TV reconstructions of the TV-phantom for 50 α values ranging from $1 \cdot 10^{-4}$ to $1 \cdot 10^0$ and 50 γ values ranging from $1 \cdot 10^{-5}$ to $1 \cdot 10^2$. The white dashed ellipse on the heatmap shows a region of α and γ values that provide nearly optimal reconstructions, i.e. with minimal NRMSD values. The ellipse width is longer than its height, which indicates that there is a large range of α values for which the reconstruction quality is close to optimal provided γ is within the same magnitude as its optimal value. For α

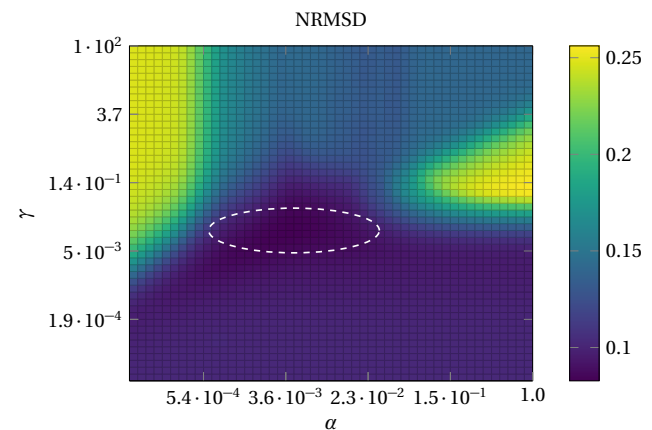


Figure 6: The NRMSD is shown for the debiased TV reconstructions of the TV-phantom for 50 α values ranging from $1 \cdot 10^{-4}$ to $1 \cdot 10^0$ and 50 γ values ranging from $1 \cdot 10^{-5}$ to $1 \cdot 10^2$, with a white dashed ellipse surrounding the region of α and γ values reconstructing images with minimal NRMSD values.

Note that the observations made so far can also be made for the ℓ^1 -phantom but are not shown here for conciseness. To this end, we consider the reconstructions of the TV-phantom and the ℓ^1 -phantom with the corresponding reconstruction method and noise scaling value of 100. Figure 7 shows the regular and the debiased reconstruction results for the TV- and ℓ^1 -phantoms for 3 different α values, which we refer to as low, medium and

high, and a fixed γ value of 0.015.

Without debiasing, one can observe that the structure of both phantoms is recovered as long as the regularization parameter is not too large. For low α values, the reconstruction is unable to produce homogeneous regions in the TV case and sharp edges in both. For medium α values, the overall visual quality of the images is best, but still a significant under-estimation of the image signal can be observed. For the ℓ^1 -phantom we observe this under-estimation for all regularization parameters, whereas we observe a shift from over-estimation at low α values to under-estimation at large α values for the TV-phantom.

The debiased reconstructions for the TV- and ℓ^1 -phantoms show that for low α values debiasing has a negative impact on the quality of the images. This is especially prominent in the case of TV regularization, where a strong over-estimation of the image signal and noise amplification occur. For α values greater than the optimal ones, the TV and ℓ^1 debiased solutions still offer a significant improvement in recovering the intensities but are still affected by the over-regularization from the first step, i.e., they do not recover parts of the phantom that are lost in the biased reconstructions. Lastly, for the medium α value, optimal debiased solutions are obtained with nearly perfect intensity recovery and an overall improvement in the structure of both phantoms.

V.IV. Bias - iron mass estimation

Figure 8 shows reconstructions for the experimental data using the two-step debiasing method for the experimental TV- and ℓ^1 -phantoms. Regular and debiased reconstructions are shown for three regularization parameters each, i.e., $\frac{1}{5}\alpha_{\text{opt}}$, α_{opt} , and $5\alpha_{\text{opt}}$. Tikhonov regularization is presented for α_{opt} only, which is the optimal regularization parameter that gives the best iron mass estimation for the medium circle and central dot of the TV- and ℓ^1 -phantom for each reconstruction, respectively. For Tikhonov regularization α_{opt} was $1 \cdot 10^{-6}$ for TV-phantom and $1 \cdot 10^{-5}$ for ℓ^1 -phantom. For TV- and ℓ^1 -phantoms, α_{opt} was equal to $5 \cdot 10^{-5}$ and $2.5 \cdot 10^{-5}$, respectively. The debiasing parameter γ was set to $1.7 \cdot 10^{-4}$ for both the TV- and ℓ^1 -phantoms. Similar visual observations regarding over- and under-regularization can be made as for the simulated data, except that bias is more prominent for the regular reconstruction of the experimental data. We notice that regular reconstructed images for both phantoms suffer from a severe drop in intensities, circles of the TV phantom are distorted and the dots of the second phantom are blurred. We also notice a similar behavior for the reconstructions with different α values (low, medium, and large) as in the simulated data reconstructions. Thus, with regular reconstruction one either gets a noisier reconstruction with smaller bias or less noise with larger bias. However, one sees in the second and fourth

	iron mass [μg]			
	TV phantom			ℓ^1 phantom
	L	M	S	
True iron mass	196	88	35	10
Tikhonov	133	62	25	0.158 - 0.278
Regular	101	44	14	0.07 - 0.18
Debiased	171	89	34	5.2 - 9.5

Table 1: This table shows the estimated iron masses for each substructure of TV-phantom and a range for all substructures of the ℓ^1 -phantom. Reconstructions were made using regular, debiased, and Tikhonov regularization with their optimal α values. For reference the true iron masses are shown in the first row.

columns of Figure 8 that the debiased reconstructions with the optimal α values have the best overall structure and intensities.

The results of the iron mass estimation within the central slice for each substructure of the phantom are summarized in Table 1. The bias introduced by the different regularization techniques leads to a systematic error in the estimation of the iron mass within these substructures. This error is largest for the regular TV and ℓ^1 regularization and less severe for the Tikhonov regularization. In both cases the true iron mass is underestimated. This under-estimation is most prominent for the ℓ^1 regularization, where the true iron mass is underestimated between 2 and 3 orders of magnitude. In comparison, we observe a much better iron mass estimation for the debiased regularization with both over- and under-estimation occurring. The best results obtained across regular, debiased and Tikhonov regularization are observed for the TV-phantom with its large homogeneous spatial structures. In detail we observe that the true iron masses are estimated to be in-between a factor of 0.68 and 0.71 of its true value for Tikhonov regularization, a factor of 0.4 and 0.52 for regular TV regularization, and a factor of 0.88 and 1.01 for the debiased TV regularization.

VI. Discussion and conclusion

In the present work, TV and ℓ^1 regularized MPI reconstruction bias was analysed and a method for its reduction was introduced. To this end, simulated data and an experimental application was considered. The proposed bias-reduction method is able to successfully reduce bias in both cases and outperforms standard Tikhonov regularization for the latter. Although only two specific sparsity promoting regularization methods were considered, the proposed debiasing method is very general and applicable to a wide range of regularization functionals.

The bias we observed in the regularized reconstructions is of two kinds. First, an incorrect estimation of

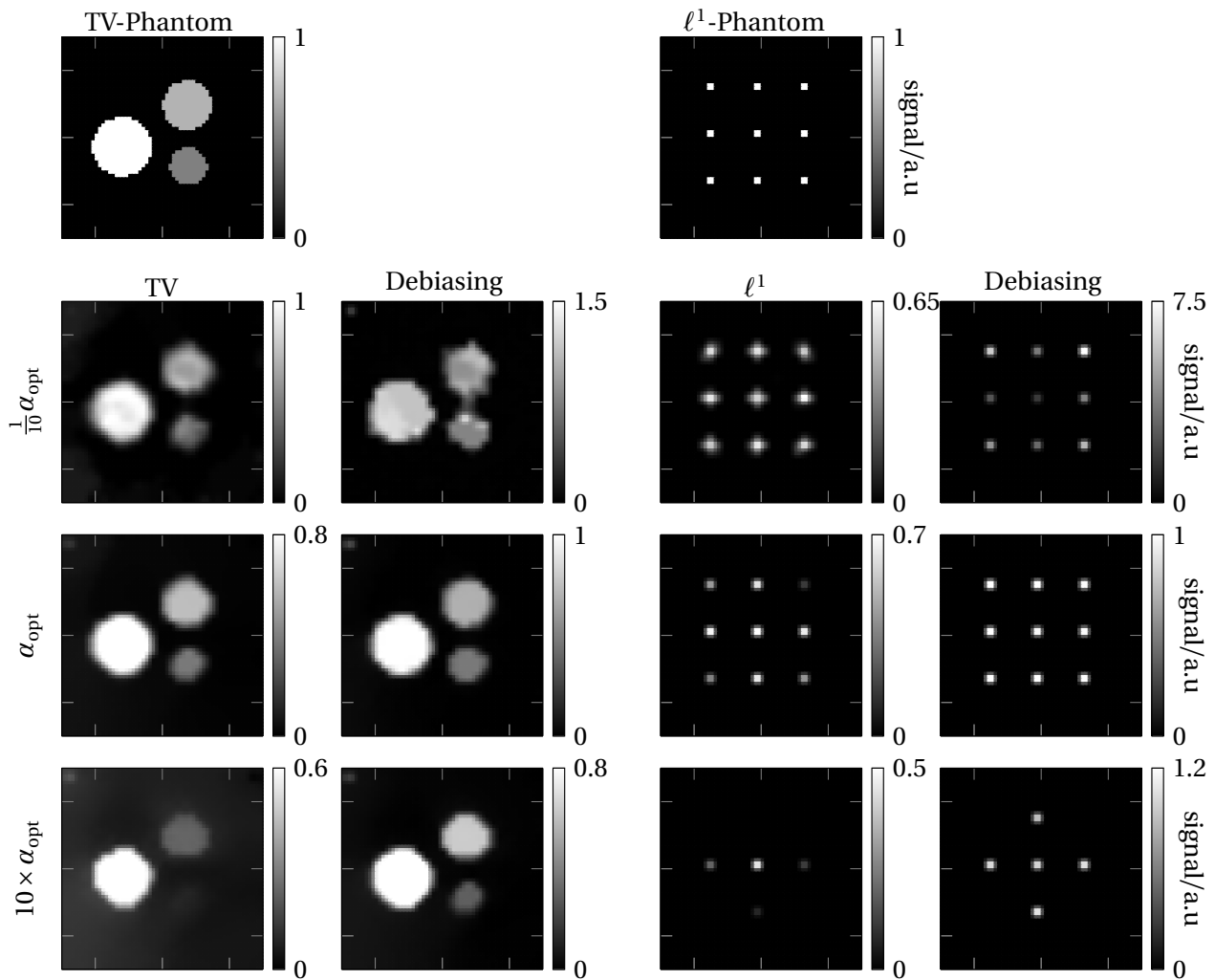


Figure 7: Reconstructions of the TV- and ℓ^1 -phantom with noise level 100 are shown on the left and right hand side of the figure. Each phantom is reconstructed using a low, medium, and large regularization parameter, without and with additional debiasing.

the signal strengths in regions with MPI tracer. Underestimation could be observed for both regularization types with a clear trend towards lower signal strengths as the regularization parameter increases. This is not surprising considering that the solution of the TV and ℓ^1 regularized MPI reconstruction tends towards zero in the limit, where the respective regularization parameter tends towards infinity. In case of TV regularization both over- and under-estimation could be observed, the former occurring for small regularization parameters. Second, we found low intensity noisy signal in regions without tracer. Due to the fact that the reconstructed MPI signal is non-negative, this leads to a systematic over-estimation of the signal in these regions. Although the strength of the bias seems to be more severe in our experimental setup, the general characteristic of the bias seems independent on the choice of simulation versus experimental setup. Note that the latter bias is also present without additional regularization terms. We therefore

attribute it to concentration vectors being restricted to the non-negative half space, which is also a form of regularization. In general bias will always be present in MPI if regularization is used, although its characteristics and strength may differ for each functional.

Our results show that the bias introduced by the TV and ℓ^1 regularization functionals can be significantly reduced by an additional debiasing step, which is adopted from [26]. This is best illustrated using our simulation setup, where the discrepancy maps and the NRMSD can be used to quantify the bias. A comparison of the discrepancy maps of regular and debiased reconstructions shows that debiasing improves the estimation of the signal strengths in regions with MPI tracer and lowers the background signal in regions without. Both improvements net in a decrease of the NRMSD values before and after debiasing as shown in Figure 5, respectively. Discrepancy map and NRMSD are not available in our experimental setup such that we restricted ourselves to a visual

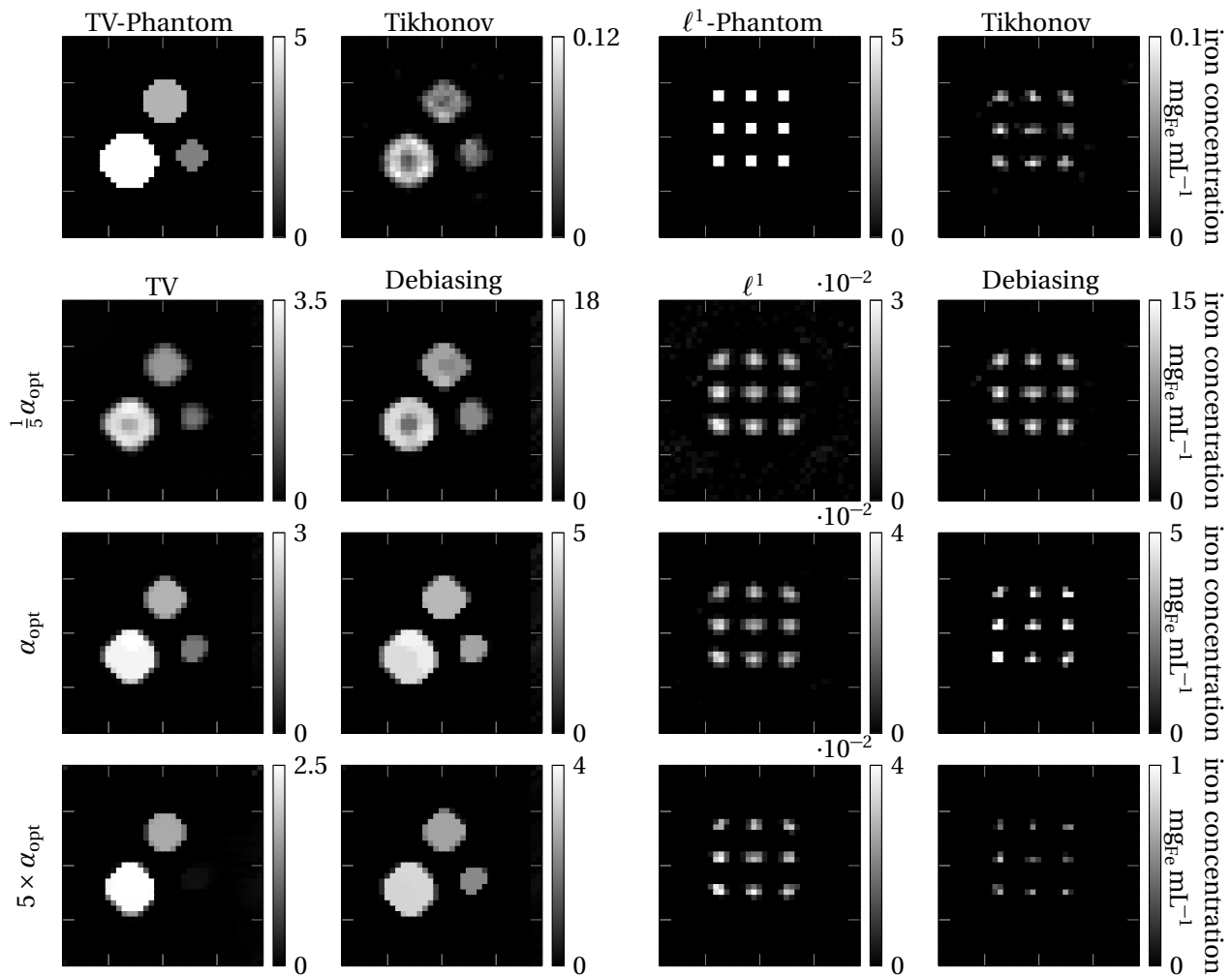


Figure 8: The central z-slice of reconstructions of the experimental TV- and ℓ^1 -phantom is shown. For reference, the phantom and Tikhonov regularized reconstructions with regularization parameter α_{opt} are shown in the top row. The remaining rows show three reconstructions done using regular TV, debiased TV, regular ℓ^1 and debiased ℓ^1 regularization from left to right. The regularization parameter is different for each of these rows with α_{opt} being the regularization parameter with the least deviation between true and estimated iron mass for the medium circle and central dot within the slice shown.

comparison of the reconstructed images in this case and a calibration method for choosing the α values that optimally quantifies the iron mass with the addition that we also compared against the commonly used Tikhonov regularization. Here too, the debiased reconstruction outperforms the regular reconstruction in terms of reconstructing the phantoms shape, structure, and estimating the signal strengths in regions with MPI tracer. Although signal estimation can have low bias for the Tikhonov reconstruction as well, as shown for the TV phantom, it is still outperformed by debiased reconstruction in terms of recovering the phantom's homogeneous structure.

How well debiasing factually decreases bias depends mostly on the choice of the regularization parameter α . In MPI this parameter is often chosen manually. A certain parameter range is investigated to find a parameter providing a good trade off between bias and noise, e.g.

based on visual inspection of the reconstructed images. In our simulation setup we mimicked this step by the automatic parameter tuning method introduced earlier and discuss these results next. We found that noisier measurements lead to larger optimal regularization parameters for all regularization functionals. This makes sense, since there is more noise to trade off. Moreover, we found that the optimal regularization parameter was not the same for debiased and regular reconstruction. Hence, the regularization parameter should be tuned independently for debiased reconstructions. However, it is noteworthy that even if the suboptimal parameter of the regular reconstruction was chosen, we observed a decrease in bias when switching to the debiased reconstruction. Consequently, this parameter could be used as starting point when searching for the optimal parameter. As best seen in our simulation setup, for small α values,

the debiased reconstruction yields larger bias than the regular reconstruction as shown in Figure 5 (a) and Figure 5 (b). For sufficiently large α values a break-even point is reached, from which on the debiased reconstruction always yields smaller bias compared to the regular one. However, this break-even point was more than an order of magnitude smaller than both the optimal debiasing and the optimal regular regularization parameter in our simulation setup such that this issue seems to be avoidable. However, since we can not make any general statements, we advice to take this issue into consideration when adopting this method.

The impact of debiasing also depends on the choice of the debiasing parameter γ . From the heatmap in Figure 6, one sees that choosing γ close to its optimal value ensures a large range of α values resulting in good reconstruction outcome. Thus, as with most regularization parameters, this choice must be done manually, dependent on the data to be reconstructed. However, as our data suggests there is a range of γ values which can provide good reconstruction outcomes. The debiasing step with this optimal γ value always offers an improvement for all possible choices of α , except for extremely small α values. For small α values, γ also needs to be chosen small to avoid making the reconstruction worse due to the noise amplification.

In this work, the estimation of the iron mass in simple technical phantoms was considered to illustrate the potential impact of bias on applications. Applications that directly benefit from a more precise iron quantification are e.g. the quantification of vascular stenosis [11, 12], or the nanoparticle core size discrimination [23]. Our results show that bias in both Tikhonov and regular TV and ℓ^1 regularization yields a systematic under-estimation of the iron mass. Most severe for the regular TV and ℓ^1 regularization and less severe for the Tikhonov regularization. In all cases the debiased regularization yielded the smallest estimation error with both over- and under-estimation of the true iron masses occurring. For the debiased ℓ^1 regularization the error is still quite large with estimated iron masses in-between 3.5 μg and 11 μg compared to the true value of 10 μg such that quantitative applications will be hard to realize in this case and we encourage further investigation of this issue. For the debiased TV regularization however, the relative estimation error is below 0.11 and more likely to be tolerable. Our results indicate that debiased regularization is the best choice for quantitative applications outperforming standard Tikhonov regularization and their non-debiased counterparts in our examples. However, Tikhonov regularization seems a solid fall back option if one finds a way to handle the systematic error, e.g. by taking it into account in a post-processing step [22].

In summary, we have shown that bias in MPI caused by regularization can manifest itself in many ways, e.g. in a systematic over- or under-estimation of the particle

distribution. Depending on the application this can lead to systematic errors, e.g. in medical applications such as the determination of stenosis degrees [12] or quantification of perfusion [14]. The debiasing technique proposed and analyzed here has been shown able to significantly reduce this issue to the point, where systematic errors might be tolerable, which makes it especially promising for MPI imaging applications that require accurate quantification of the particle distribution.

References

- [1] B. Gleich and J. Weizenecker. Tomographic imaging using the nonlinear response of magnetic particles. *Nature*, 435(7046):1214–1217, 2005, doi:[10.1038/nature03808](https://doi.org/10.1038/nature03808).
- [2] T. Knopp and T. M. Buzug. *Magnetic Particle Imaging: An Introduction to Imaging Principles and Scanner Instrumentation*. Berlin, Heidelberg: Springer Berlin Heidelberg, 2012, doi:[10.1007/978-3-642-04199-0](https://doi.org/10.1007/978-3-642-04199-0).
- [3] J. Weizenecker, B. Gleich, J. Rahmer, H. Dahnke, and J. Borgert. Three-dimensional real-time in vivo magnetic particle imaging. *Physics in Medicine and Biology*, 54(5):L1–L10, 2009, doi:[10.1088/0031-9155/54/5/L01](https://doi.org/10.1088/0031-9155/54/5/L01).
- [4] T. Knopp, S. Biederer, T. Sattel, and T. M. Buzug. Singular value analysis for Magnetic Particle Imaging, in *2008 IEEE Nuclear Science Symposium Conference Record*, 4525–4529, IEEE, 2008, doi:[10.1109/NSSMIC.2008.4774296](https://doi.org/10.1109/NSSMIC.2008.4774296).
- [5] W. Erb, A. Weinmann, M. Ahlborg, C. Brandt, G. Bringout, T. M. Buzug, J. Frikel, C. Kaethner, T. Knopp, T. März, M. Möddel, M. Storath, and A. Weber. Mathematical analysis of the 1D model and reconstruction schemes for magnetic particle imaging. *Inverse Problems*, 34(5):055012, 2018, doi:[10.1088/1361-6420/aab8d1](https://doi.org/10.1088/1361-6420/aab8d1).
- [6] T. Kluth, B. Jin, and G. Li. On the degree of ill-posedness of multi-dimensional magnetic particle imaging. *Inverse Problems*, 34(9):095006, 2018, doi:[10.1088/1361-6420/aad015](https://doi.org/10.1088/1361-6420/aad015).
- [7] T. A. Johansen. On Tikhonov regularization, bias and variance in nonlinear system identification. *Automatica*, 33(3):441–446, 1997, doi:[10.1016/S0005-1098\(96\)00168-9](https://doi.org/10.1016/S0005-1098(96)00168-9).
- [8] M. Benning and M. Burger. Modern regularization methods for inverse problems. *Acta Numerica*, 27:1–111, 2018, doi:[10.1017/S0962492918000016](https://doi.org/10.1017/S0962492918000016).
- [9] M. Storath, C. Brandt, M. Hofmann, T. Knopp, J. Salamon, A. Weber, and A. Weinmann. Edge Preserving and Noise Reducing Reconstruction for Magnetic Particle Imaging. *IEEE Transactions on Medical Imaging*, 36(1):74–85, 2017, doi:[10.1109/TMI.2016.2593954](https://doi.org/10.1109/TMI.2016.2593954).
- [10] C. Bathke, T. Kluth, C. Brandt, and P. Maaß. Improved image reconstruction in magnetic particle imaging using structural a priori information. *International Journal on Magnetic Particle Imaging*, 3(1), 2017, doi:[10.18416/IJMPL.2017.1703015](https://doi.org/10.18416/IJMPL.2017.1703015).
- [11] S. Herz, P. Vogel, T. Kampf, M. A. Ruckert, S. Veldhoen, V. C. Behr, and T. A. Bley. Magnetic Particle Imaging for Quantification of Vascular Stenoses: A Phantom Study. *IEEE Transactions on Medical Imaging*, 37(1):61–67, 2018, doi:[10.1109/TMI.2017.2717958](https://doi.org/10.1109/TMI.2017.2717958).
- [12] S. Vaalma, J. Rahmer, N. Panagiotopoulos, R. L. Duschka, J. Borgert, J. Barkhausen, F. M. Vogt, and J. Haegele. Magnetic Particle Imaging (MPI): Experimental Quantification of Vascular Stenosis Using Stationary Stenosis Phantoms. *PLOS ONE*, 12(1):e0168902B. Xu, Ed., 2017, doi:[10.1371/journal.pone.0168902](https://doi.org/10.1371/journal.pone.0168902).
- [13] X. Y. Zhou, K. E. Jeffris, E. Y. Yu, B. Zheng, P. W. Goodwill, P. Nahid, and S. M. Conolly. First in vivo magnetic particle imaging of lung perfusion in rats. *Physics in Medicine and Biology*, 62(9):3510–3522, 2017, doi:[10.1088/1361-6560/aa616c](https://doi.org/10.1088/1361-6560/aa616c).

- [14] P. Ludewig, N. Gdaniec, J. Sedlacik, N. D. Forkert, P. Szwargulski, M. Graeser, G. Adam, M. G. Kaul, K. M. Krishnan, R. M. Ferguson, A. P. Khandhar, P. Walczak, J. Fiehler, G. Thomalla, C. Gerloff, T. Knopp, and T. Magnus. Magnetic Particle Imaging for Real-Time Perfusion Imaging in Acute Stroke. *ACS Nano*, 11(10):10480–10488, 2017, doi:[10.1021/acsnano.7b05784](https://doi.org/10.1021/acsnano.7b05784).
- [15] M. Graeser, F. Thieben, P. Szwargulski, F. Werner, N. Gdaniec, M. Boberg, F. Griese, M. Möddel, P. Ludewig, D. van de Ven, O. M. Weber, O. Woywode, B. Gleich, and T. Knopp. Human-sized magnetic particle imaging for brain applications. *Nature Communications*, 10(1):1936, 2019, doi:[10.1038/s41467-019-09704-x](https://doi.org/10.1038/s41467-019-09704-x).
- [16] J. Sedlacik, A. Frölich, J. Spallek, N. D. Forkert, T. D. Faizy, F. Werner, T. Knopp, D. Krause, J. Fiehler, and J.-H. Buhk. Magnetic Particle Imaging for High Temporal Resolution Assessment of Aneurysm Hemodynamics. *PLOS ONE*, 11(8):e0160097J. Sznitman, Ed., 2016, doi:[10.1371/journal.pone.0160097](https://doi.org/10.1371/journal.pone.0160097).
- [17] M. G. Kaul, J. Salamon, T. Knopp, H. Itrich, G. Adam, H. Weller, and C. Jung. Magnetic particle imaging for in vivo blood flow velocity measurements in mice. *Physics in Medicine & Biology*, 63(6):064001, 2018, doi:[10.1088/1361-6560/aab136](https://doi.org/10.1088/1361-6560/aab136).
- [18] J. W. M. Bulte, P. Walczak, M. Janowski, K. M. Krishnan, H. Arami, A. Halkola, B. Gleich, and J. Rahmer. Quantitative “Hot-Spot” Imaging of Transplanted Stem Cells Using Superparamagnetic Tracers and Magnetic Particle Imaging. *Tomography*, 1(2):91–97, 2015, doi:[10.18383/j.tom.2015.00172](https://doi.org/10.18383/j.tom.2015.00172).
- [19] C. Z. Cooley, J. B. Mandeville, E. E. Mason, E. T. Mandeville, and L. L. Wald. Rodent Cerebral Blood Volume (CBV) changes during hypercapnia observed using Magnetic Particle Imaging (MPI) detection. *NeuroImage*, 178:713–720, 2018, doi:[10.1016/j.neuroimage.2018.05.004](https://doi.org/10.1016/j.neuroimage.2018.05.004).
- [20] J. Rahmer, A. Halkola, B. Gleich, I. Schmale, and J. Borgert. First experimental evidence of the feasibility of multi-color magnetic particle imaging. *Physics in Medicine and Biology*, 60(5):1775–91, 2015, doi:[10.1088/0031-9155/60/5/1775](https://doi.org/10.1088/0031-9155/60/5/1775).
- [21] C. Stehning, B. Gleich, and J. Rahmer. Simultaneous magnetic particle imaging (MPI) and temperature mapping using multi-color MPI. *International Journal on Magnetic Particle Imaging*, 2(2), 2016, doi:[10.18416/IJMPI.2016.1612001](https://doi.org/10.18416/IJMPI.2016.1612001).
- [22] M. Möddel, C. Meins, J. Dieckhoff, and T. Knopp. Viscosity quantification using multi-contrast magnetic particle imaging. *New Journal of Physics*, 20(8):083001, 2018, doi:[10.1088/1367-2630/aad44b](https://doi.org/10.1088/1367-2630/aad44b).
- [23] C. Shasha, E. Teeman, K. M. Krishnan, P. Szwargulski, T. Knopp, and M. Möddel. Discriminating nanoparticle core size using multi-contrast MPI. *Physics in Medicine & Biology*, 64(7):074001, 2019, doi:[10.1088/1361-6560/ab0fc9](https://doi.org/10.1088/1361-6560/ab0fc9).
- [24] K. N. Tapp, W. B. Lea, M. S. Johnson, M. Tann, J. W. Fletcher, and G. D. Hutchins. The Impact of Image Reconstruction Bias on PET/CT 90 Y Dosimetry After Radioembolization. *Journal of Nuclear Medicine*, 55(9):1452–1458, 2014, doi:[10.2967/jnumed.113.133629](https://doi.org/10.2967/jnumed.113.133629).
- [25] A. Weber, F. Werner, J. Weizenecker, T. M. Buzug, and T. Knopp. Artifact free reconstruction with the system matrix approach by overscanning the field-free-point trajectory in magnetic particle imaging. *Physics in Medicine and Biology*, 61(2):475–487, 2016, doi:[10.1088/0031-9155/61/2/475](https://doi.org/10.1088/0031-9155/61/2/475).
- [26] E.-M. Brinkmann, M. Burger, J. Rasch, and C. Sutour. Bias Reduction in Variational Regularization. *Journal of Mathematical Imaging and Vision*, 59(3):534–566, 2017, doi:[10.1007/s10851-017-0747-z](https://doi.org/10.1007/s10851-017-0747-z).
- [27] J. Rahmer, J. Weizenecker, B. Gleich, and J. Borgert. Signal encoding in magnetic particle imaging: properties of the system function. *BMC Medical Imaging*, 9:4, 2009, doi:[10.1186/1471-2342-9-4](https://doi.org/10.1186/1471-2342-9-4).
- [28] M. Grüttner, T. Knopp, J. Franke, M. Heidenreich, J. Rahmer, A. Halkola, C. Kaethner, J. Borgert, and T. M. Buzug. On the formulation of the image reconstruction problem in magnetic particle imaging. *Biomedizinische Technik/Biomedical Engineering*, 58(6), 2013, doi:[10.1515/bmt-2012-0063](https://doi.org/10.1515/bmt-2012-0063).
- [29] L. I. Rudin, S. Osher, and E. Fatemi. Nonlinear total variation based noise removal algorithms. *Physica D: Nonlinear Phenomena*, 60(1-4):259–268, 1992, doi:[10.1016/0167-2789\(92\)90242-F](https://doi.org/10.1016/0167-2789(92)90242-F).
- [30] B. Jin and P. Maass. Sparsity regularization for parameter identification problems. *Inverse Problems*, 28(12):123001, 2012, doi:[10.1088/0266-5611/28/12/123001](https://doi.org/10.1088/0266-5611/28/12/123001).
- [31] M. Burger, Bregman Distances in Inverse Problems and Partial Differential Equations, in 2016, 3–33. doi:[10.1007/978-3-319-30785-5_2](https://doi.org/10.1007/978-3-319-30785-5_2).
- [32] E. Esser, X. Zhang, and T. F. Chan. A General Framework for a Class of First Order Primal-Dual Algorithms for Convex Optimization in Imaging Science. *SIAM Journal on Imaging Sciences*, 3(4):1015–1046, 2010, doi:[10.1137/09076934X](https://doi.org/10.1137/09076934X).
- [33] A. Chambolle and T. Pock. A First-Order Primal-Dual Algorithm for Convex Problems with Applications to Imaging. *Journal of Mathematical Imaging and Vision*, 40(1):120–145, 2011, doi:[10.1007/s10851-010-0251-1](https://doi.org/10.1007/s10851-010-0251-1).
- [34] R. T. Rockafellar, Convex Analysis. Princeton University Press, 1970, doi:[10.1515/9781400873173](https://doi.org/10.1515/9781400873173).
- [35] J. Peypouquet, Convex Optimization in Normed Spaces, ser. SpringerBriefs in Optimization. Cham: Springer International Publishing, 2015, doi:[10.1007/978-3-319-13710-0](https://doi.org/10.1007/978-3-319-13710-0).
- [36] A. Beck, First-Order Methods in Optimization. Philadelphia, PA: Society for Industrial and Applied Mathematics, 2017, doi:[10.1137/1.9781611974997](https://doi.org/10.1137/1.9781611974997).
- [37] K. Them, M. G. Kaul, C. Jung, M. Hofmann, T. Mummert, F. Werner, and T. Knopp. Sensitivity Enhancement in Magnetic Particle Imaging by Background Subtraction. *IEEE Transactions on Medical Imaging*, 35(3):893–900, 2016, doi:[10.1109/TMI.2015.2501462](https://doi.org/10.1109/TMI.2015.2501462).
- [38] J. Weizenecker, J. Borgert, and B. Gleich. A simulation study on the resolution and sensitivity of magnetic particle imaging. *Physics in Medicine and Biology*, 52(21):6363–6374, 2007, doi:[10.1088/0031-9155/52/21/001](https://doi.org/10.1088/0031-9155/52/21/001).
- [39] T. Knopp, T. Viereck, G. Bringout, M. Ahlberg, A. von Gladiss, C. Kaethner, A. Neumann, P. Vogel, J. Rahmer, and M. Möddel. MDF: Magnetic Particle Imaging Data Format. *ArXiv e-prints*, 2018. arXiv: [1602.06072](https://arxiv.org/abs/1602.06072). URL: <https://arxiv.org/abs/1602.06072>.
- [40] T. Knopp, P. Szwargulski, F. Griese, and M. Gräser. OpenMPIData: An initiative for freely accessible magnetic particle imaging data. *Data in Brief*, 28:104971, 2020, doi:[10.1016/j.dib.2019.104971](https://doi.org/10.1016/j.dib.2019.104971).
- [41] J. Bezanson, A. Edelman, S. Karpinski, and V. B. Shah. Julia: A Fresh Approach to Numerical Computing. *SIAM Review*, 59(1):65–98, 2017, doi:[10.1137/141000671](https://doi.org/10.1137/141000671).
- [42] T. Knopp, P. Szwargulski, F. Griese, M. Grosser, M. Boberg, and M. Möddel. MPIReco.jl: Julia Package for Image Reconstruction in MPI. *International Journal on Magnetic Particle Imaging*, 5(1-2), 2019, doi:[10.18416/IJMPI.2019.1907001](https://doi.org/10.18416/IJMPI.2019.1907001).